# Phonon-coupled ultrafast interlayer charge oscillation at van der Waals heterostructure interfaces

Qijing Zheng, Yu Xie, Zhenggang Lan, Oleg V. Prezhdo, Wissam A. Saidi, and Jin Zhao

Phys. Rev. B **97**, 205417 — Published 14 May 2018

DOI: 10.1103/PhysRevB.97.205417

# Phonon Coupled Ultrafast Interlayer Charge Oscillation at Van Der Waals Heterostructure Interfaces

*Qijing Zheng,[1] Yu Xie,[2] Zhenggang Lan,[2] Oleg V. Prezhdo,[3] Wissam A. Saidi,[4] and Jin Zhao[1,5,6]**

[1] ICQD/Hefei National Laboratory for Physical Sciences at Microscale, and Key Laboratory of Strongly-Coupled Quantum Matter Physics, Chinese Academy of Sciences, and Department of Physics, University of Science and Technology of China, Hefei, Anhui 230026, China

[2]Key Laboratory of Biobased Materials, Qingdao Institute of Bioenergy and Bioprocess Technology, Chinese Academy of Sciences, Qingdao, Shandong 266101, China

[3]Departments of Chemistry, and Physics and Astronomy, University of Southern California, Los Angeles, CA 90089, United States

[4]Department of Mechanical Engineering and Materials Science, University of Pittsburgh, Pittsburgh, Pennsylvania 15261, United States

[5]Department of Physics and Astronomy, University of Pittsburgh, Pittsburgh PA 15260, United States

[6]Synergetic Innovation Center of Quantum Information & Quantum Physics, University of Science and Technology of China, Hefei, Anhui 230026, China

## Abstract

Van der Waals (vdW) heterostructures of transition-metal dichalcogenide (TMD) semiconductors are central not only for fundamental science, but also for electro- and optical-device technologies where the interfacial charge transfer is a key factor. Ultrafast interfacial charge dynamics has been intensively studied, however, the atomic scale insights into the effects of the electron-phonon (*e-p*) coupling are still lacking. In this report, using time dependent *ab initio* non-adiabatic molecular dynamics (NAMD), we study the ultrafast interfacial charge transfer dynamics of two different TMD heterostructures $MoS_2/WS_2$ and $MoSe_2/WSe_2$, which have similar band structures but different phonon frequencies. We found that $MoSe_2/WSe_2$ has softer phonon modes compared to $MoS_2/WS_2$, and thus phonon-coupled charge oscillation can be excited with sufficient phonon excitations at room temperature. In contrast, for $MoS_2/WS_2$, phonon-coupled interlayer charge oscillations are not easily excitable. Our study provides an atomic level understanding on how the phonon excitation and *e-p* coupling affect the interlayer charge transfer dynamics, which is valuable for both the fundamental understanding of ultrafast dynamics at vdW hetero-interfaces and the design of novel quasi-2D devices for optoelectronic and photovoltaic applications.

* Email: zhaojin@ustc.edu.cn

## Introduction

Van der Waals (vdW) heterostructures composed of two-dimensional (2D) transition metal dichalcogenides (TMDs) have optical band gaps in the visible spectral region and strong light-matter interactions.[1-7] This makes them of potential interest to different applications in the field of electronics, optoelectronics and energy-harvesting.[2, 3, 8-14]

For the applications in solar energy conversion and optoelectronics, efficient charge separation is a key factor, which can be accomplished by fast interlayer charge transfer. Most vertically-stacked TMD heterostructures show type II band alignment where the conduction band minimum (CBM) and the valence band maximum (VBM) reside on different layers.[15-19] Such feature facilitates the electron-hole separation after a photoexcitation, and consequently, increases the photocarrier lifetime. However, fast carrier transport is typically associated with materials with strong chemical bonding rather than with materials that have atomically sharp interfaces and are bound by vdW forces, as in the case of TMD heterostructures. Furthermore, excitons in single layer TMDs have large binding energies of the order of 0.6 - 1.0 eV, and their wave functions are localized in 2D.[4, 5, 20-22] These factors are expected to inhibit interlayer charge transfer in the TMDs.

There have been intensive investigations to understand the interlayer charge transfer dynamics in TMD heterostructures recently.[9, 23-29] Contrary to common expectations, ultrafast interlayer charge transfer has been experimentally observed in different TMD heterostructures.[9, 23-25] For example, Hong et al. used resonant femtosecond pump pulse to selectively excite intralayer excitons in $MoS_2$, and transient absorption to probe the subsequent charge transfer. This study found that the holes quickly transfer to $WS_2$ layer due to the type II band alignment, whereas electrons remain in the $MoS_2$ layer, forming an interlayer exciton. The transient absorption signals from the photoexcited electrons in $MoS_2$ and holes in $WS_2$ had a rise time within 50 fs. In other transient absorption measurements on $MoS_2/MoSe_2$, Ceballos et al. also found an instrument limited time scale of less than 200 fs for both the hole and electron transfer.[23] Moreover, Zhu et al. reported an efficient quenching of photo-luminescence from intralayer exciton to interlayer exciton by the interlayer charge transfer when a $MoS_2/WSe_2$ heterojunction is formed.[24]

It is essential to understand the unexpected ultrafast interfacial charge transfer at atomic scale. As already shown in some of the investigations on ultrafast carrier dynamics in TMD systems,[28, 30] the dynamics of electrons are naturally coupled to the motion of nuclei, namely, the phonons. The development of time-dependent non-adiabatic molecular dynamics (NAMD) makes it possible to investigate the excited carrier dynamics and their coupling to phonons using state-of-the-art *ab initio* calculations.[31] Combined time-dependent DFT (TDDFT) with fewest switches surface hopping (FSSH) scheme, the excited carrier dynamics have been investigated in different condensed matter systems.[32-35] We have used this method to investigate the time-dependent excited carrier dynamics at various surfaces and interfaces.[28, 36, 37] In our recent work, the phonon-assistant ultrafast excited hole transfer at $MoS_2/WS_2$ is revealed.[28] In order to systematically understand how the electron-phonon (*e-p*) coupling affect the ultrafast carrier dynamics at TMD interface, we use *ab initio* non-adiabatic molecular dynamics (NAMD) to investigate the excited interfacial electron transfer at two different TMD heterostructures $MoS_2/WS_2$ and $MoSe_2/WSe_2$. These two different TMD heterostructures have similar band structures but different phonon frequencies. It is found that for both of them, the electron transfer is mostly coupled with the $A_1$ intralayer optical phonon mode. By replacing S with Se, $A_1$ phonon mode is soften in $MoSe_2/WSe_2$ and therefore more phonons can be easily excited at room temperature. Such sufficient phonon excitation can drive electron oscillation between $MoSe_2/WSe_2$. When temperature is reduced from room temperature to 100 K, such charge oscillation is suppressed along with the phonon frozen. In contrast, in $MoS_2/WS_2$, the phonons have relatively high frequencies that are not easily excited at room temperature. Therefore, the phonon-coupled electron oscillation is not observed. The atomic level insights into how the exciton binding and *e-p* coupling affect the carrier dynamics at vdW TMD heterostructure interface is not only valuable for the fundamental understanding of the ultrafast interface charge transfer, but also provide a new strategy for the design of novel quasi-2D devices for optoelectronic and photovoltaic applications.

# METHODOLOGY

The *ab initio* NAMD simulations are carried out using home-made code Hefei-NAMD [38] which augments the Vienna *ab initio* simulation package (VASP)[39-42] with the NAMD capabilities within TDDFT and FSSH similar to ref. [32, 43, 44]. This approach is computationally tractable and has been utilized in several studies of the relaxation progress of photo-generated carriers in semiconducting materials.[33, 36] The electron-nuclear interactions are described using projector augmented wave (PAW) method.[45] We use the Perdew-Burke-Ernzerhof (PBE) exchange-correlation functional in all calculations.[46] VdW interactions are included in the simulations using the D2 approach.[47] The TMD heterostructures are modeled using an orthogonal 3×3 supercell with 108 atoms with Brillouin Zone (BZ) sampled at the Γ point. The optimized lattice constants of $MoS_2$ and $WS_2$ monolayer are identical to the third number after the decimal point i.e. 3.185 Å. For $MoSe_2$ and $WSe_2$, the optimized lattice constants are 3.320 and 3.318 Å, respectively. We use the lattice constants of 3.185 and 3.320 Å for $MoS_2/WS_2$ and $MoSe_2/WSe_2$. Seven irreducible K points including the Γ and K points of the primitive cell BZ are included and can be assigned by unfolding the energy bands.[48] The electronic structure is calculated using the optimized geometry at 0 K. After the geometry optimization, we use velocity rescaling to bring the temperature of the system to either 300 or 100 K; a 5 ps microcanonical *ab initio* molecular dynamics trajectory is then generated with a time step of 1 fs. The NAMD results are obtained by averaging over 100 different initial configurations chosen randomly from the first 3 ps of the molecular dynamics trajectory. For each chosen structure, we sample $2\times10^4$ NAMD trajectories 2 ps in length.

The extent of charge transfer from one TMD layer to another is computed by integrating the photo-excited carrier density over the region of the simulated cell occupied by one of the TMD layer, e.g. $WS_2$,

$$\int \rho(r,t)dr = \int |\psi(r,t)|^2 dr = \sum_{i,j} c_i^*(t)\, c_j(t) \int \varphi_i^*[r,R(t)]\varphi_j[r,R(t)]\, dr \qquad (1)$$

where $\rho$ is the photo-excited charge density, $\psi$ is the total wave function, which can be expanded into the Kohn-Sham wave functions $\varphi_i$ and $\varphi_j$ with $c_i$ and $c_j$ as the coefficients. The coefficients represent the occupation of excited carriers on Kohn-Sham orbitals. Taking the time-derivative of Eq. (1) gives the expression for adiabatic (AD) and non-adiabatic (NA) contribution to charge transfer:

$$\frac{d\int \rho(r,t)dr}{dt} = \sum_{ij}\left\{\frac{d\left(c_i^* c_j\right)}{dt}\int \varphi_i^*\,\varphi_j dr + c_i^* c_j \frac{d\int \varphi_i^* \varphi_j dr}{dt}\right\} \qquad (2)$$

The change in the charge density described by the first term on the right hand side of Eq. (2) is due to change of state occupation of the adiabatic KS states, which we refer to as non-adiabatic transition term. The second term describes effects due to changes of localization of the KS adiabatic state, hence the name adiabatic transfer. The contribution to the total charge transfer is obtained by further integrating the two terms on the right hand side of Eq. (2). The more details of the calculation methods can be found in the Supplemental Material.[39, 42-44, 46, 48-50] The discussion of spin orbital coupling effects, stacking effects, K-grid effects and different functional effects are also included in the Supplemental Material.[5, 19, 48, 51-55]

## Results and Discussion

### A. Electronic structure

We choose the most stable C7 stacking to investigate.[19] Before describing the NAMD results, we first inspect the electronic band structures of the $MoS_2/WS_2$ and $MoSe_2/WSe_2$ using the primitive cell with (11×11×1) K points as shown in Fig. 1 (a-b). As can be seen, the band structures of these two heterostructures show significant similarities. Both of them have type II band alignment. Valence band maximum (VBM) and conduction band minimum (CBM) are located on $WX_2$ (X=S, Se) @Γ and $MoX_2$@K respectively. As indicted by the color strip in Fig. 1 and the corresponding orbital distributions, the orbital hybridization varies with the momentum within a band. For conduction bands (CBs) at the K point, the interlayer hybridization is weak because the dominant metal $d_{xy}$ and $d_{x^2-y^2}$ and S (Se) $p_x$ and $p_y$ orbitals are mostly localized within the TMD layer. There is another local energy minimum in the CB of $MoX_2$, which is located midway along the T path between Γ and K (noted as $MX_2$@T). The interlayer hybridization at this point is relatively stronger. In this report we focus on the electron dynamics schematically shown in Fig. 1 (c). The intralayer exciton is firstly excited at $WX_2$@K, and subsequently the excited electron transfers to $MoX_2$. In the latter process, the scattering with phonon is required. Recent experimental measurements proved that the interlayer exciton formation in $MoX_2/WX_2$ with both electron and hole localized at K/K' points in momentum space.[56-59] Therefore in this investigation we consider the excited hole remains at K point in the valance band of $WX_2$ ($WX_2$@K_VB), and the intralayer exciton converts into an interlayer exciton after the electron transfer. The electron transfer route can be through $WX_2$@K directly to $MoX_2$@K. It can also transfer from $WX_2$@K first to $MoX_2$@T, and then relax to $MoX_2$@K which is the CBM. In all the investigations we take the energy of $WX_2$@K_VB, where the excited hole located, as the energy reference.

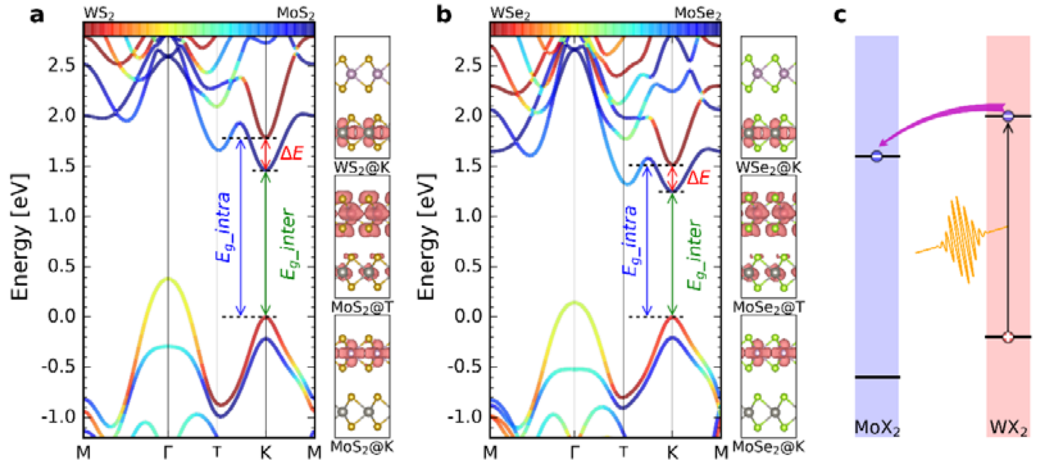

Figure 1. Band structures and orbital spatial distributions of (a) $MoS_2/WS_2$ and (b) $MoSe_2/WSe_2$ heterostructures. The energy of $WX_2$@K_VB is set to zero. The color strip indicates the localization of the states. The photoexcitation and the initial electron/hole distribution is indicated in (a-b). The schematic of electron transfer in TMD heterostructure is shown in (c).

### B. Thermal Fluctuations of the CB states

We focus on the electronic states that are involved in the dynamics near CBM considering that we are investigating the electron transfer at TMD heterostructure interface. The energy evolution of the states near CBM for $MoX_2/WX_2$ at 300 and 100 K are shown in Fig. 2 (a-d). Here we use the same color map as in Fig. 1 to show the orbitals localization. Because we are using an orthogonal 3×3 supercell, the two degenerate states at T and K points of the optimum structure become non-degenerate during the molecular dynamics. For both systems, CB states at $MoX_2$@K and $WX_2$@K are represented by the deep blue and red lines. The hybridized $MoX_2$@T states are represented by light blue lines in between the two states.

Electron-phonon coupling induces the oscillation of the Kohn-Sham eigen-energies as shown in Fig. 2 (a-d). First, for both systems, the energy oscillation at 300 K is stronger than that at 100 K, because more phonons are thermally excited at 300 K. Second, comparing $MoS_2/WS_2$ with $MoSe_2/WSe_2$, one can find that at the same temperature the oscillation amplitudes of $MoSe_2/WSe_2$ eigen-energies are much larger. In order to understand this, we performed Fourier transform (FT) of the time evolution of selected states ($MoX_2$@K, $MoX_2$@T and $WX_2$@K) for the two heterostructures at 300 and 100 K, as can be seen in Fig. 2 (e-h). For $MoS_2/WS_2$, the major peaks appear around 400 $cm^{-1}$ at both temperatures, whereas they redshift to about 230 $cm^{-1}$ in $MoSe_2/WSe_2$. In $MoSe_2/WSe_2$, at 100 K the peak around 350 $cm^{-1}$ has higher intensity than that at 300 K. This might be due to the different initial phonon excitations in the molecular dynamics at 100 and 300 K. By comparing the peak positions with Raman scattering experiments and first principle calculations,[51, 60-62] we are able to attribute the major peaks in both systems to the $A_1$ vibration mode. The redshift in $MoSe_2/WSe_2$ is due to different chalcogen masses and chemical bond strengths. Based on the analysis above, we propose that $A_1$ is the major mode coupled with the electronic states near CBM. More photons will be excited in $MoSe_2/WSe_2$ than that of $MoS_2/WSe_2$ at the same temperature because $A_1$ is much softer in the former case, which results in the observed stronger energy oscillations.

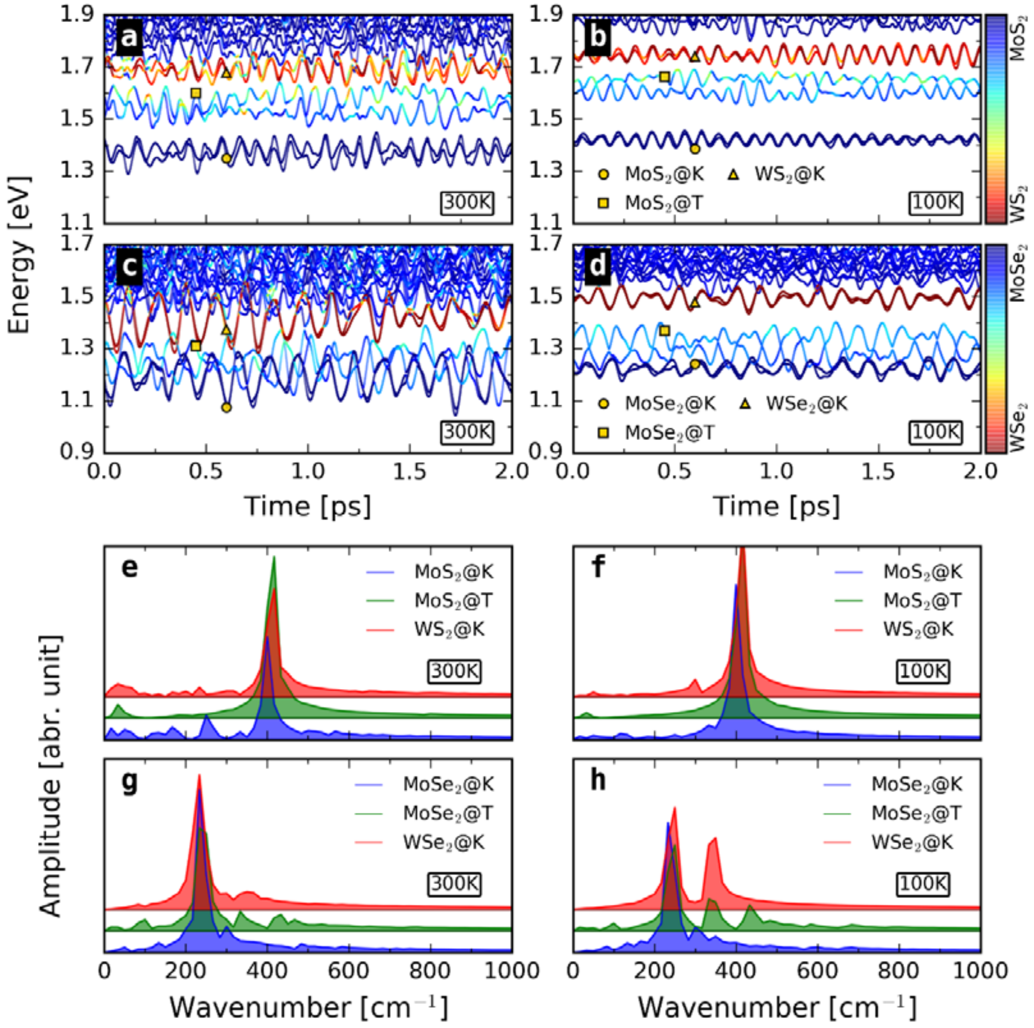

Figure 2. Time evolutions of the energy states near CBM (a-d) and FT spectrum of the selected states (e-h) of $MoX_2/WX_2$ (X=S, Se) heterostructures at 300 and 100 K. The energy reference in (a-d) is the averaged energy of $WX_2$@K_VB, and the color map shows the orbital localization.

### C. Phonon-coupled charge oscillations

We then proceed to investigate the electron transfer process at the heterostructure interface with NAMD, starting with $MoSe_2/WSe_2$. The photoexcited electron was initially populated at $WSe_2$@K state, and the results are shown in Fig. 3. Time-dependent electron transfer between the two layers can be obtained from NAMD calculations by projecting the electron localization onto the $MoSe_2$ and $WSe_2$ layers, as is shown in Fig. 3 (a-b). Moreover, time-dependent electron energy changes can also be deduced by evaluating the electron probability distribution for selected energy states from NAMD, as can be seen in Fig. 3 (c-d). By comparing the time-dependent localization and energy, the electron relaxation route in both real and momentum spaces can be obtained.

At 300 K, the electron localization on the $WSe_2$ layer [red line in Fig. 3 (a)] decreases from 90% to 10%, and the electron energy [dashed line in Fig. 3 (c)] drops to CBM within 1000 fs. From Fig. 3 (a) it is interesting to see that the interlayer charge transfer is accompanied by a charge oscillation with a damped amplitude during the first 400 fs. We notice that the period of such an oscillation is roughly the same as that of the $A_1$ mode. In the momentum space, such an oscillatory charge transfer process happens between $WSe_2$@K and $MoSe_2$@T, followed by an intralayer charge relaxation from $MoSe_2$@T to $MoSe_2$@K. Both of these processes are intervalley charge transfer, and we propose that the phonons play a crucial role here.

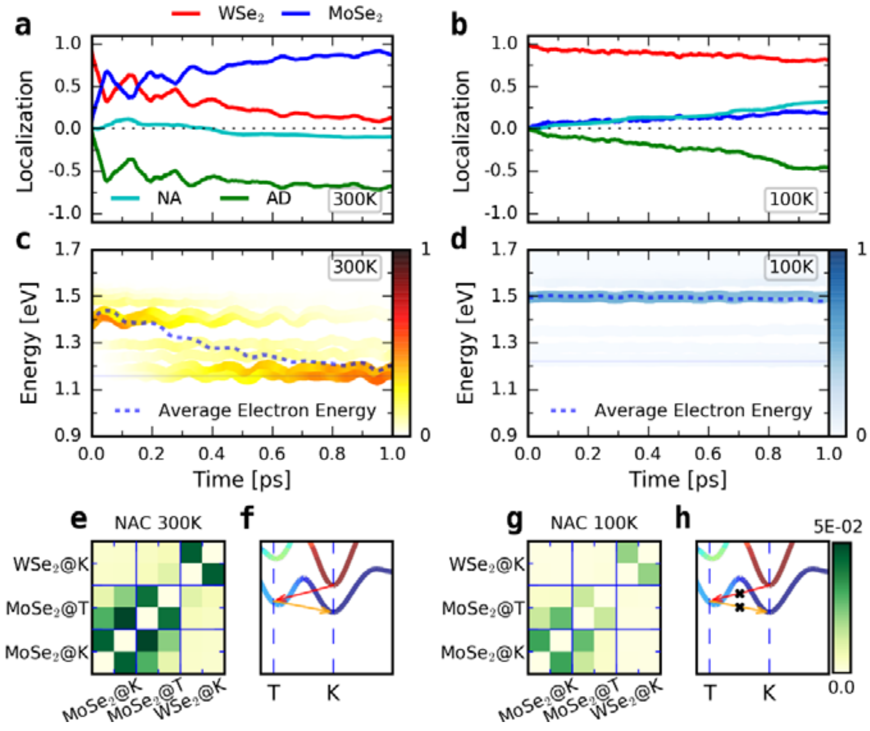

Figure 3. Non-adiabatic molecular dynamics results of $MoSe_2/WSe_2$ at 300 and 100 K, respectively. (a-b) Time-dependent electron spatial localization and (c-d) electron energy change at 300 and 100 K. In the upper part of (a-b) the red and blue lines shows the spatial electron localization on $WSe_2$ and $MoSe_2$ and in the lower part the green and cyan lines show the AD and NA contributions of the electron transfer. The color strips in (c-d) indicate electron distribution among different states and the dashed lines represent the averaged electron energy. The energy reference in (c-d) is the averaged energy of $WX_2$@K_VB while the average energy of $MoX_2/WX_2$ CBM is indicated by the horizontal line. (e) and (g) show the averaged non-adiabatic couplings (NAC) along 2 ps NAMD trajectory at 300 and 100 K. (f) and (h) show schematics of the electron relaxation route in the momentum space.

In order to understand the origin of this charge oscillation and how the phonons play a role here, we decompose the charge transfer into two parts: adiabatic (AD) and non-adiabatic (NA) charge transfer. As we discuss in the methodology part, AD charge transfer is provoked by nuclear motion that causes energy states to mix. This is naturally coupled with phonons. AD charge transfer always happens when two electronic states cross each other. In contrast, NA charge transfer involves direct charge hopping or tunneling between different states. As is indicated by the green line in Fig. 3 (a), the charge oscillation in the first 400 fs and the following intralayer charge relaxation are mainly contributed by AD process at 300 K, implying the important role of phonons.

To better reveal the effects of phonons, we investigate the same charge transfer process at a lower temperature of 100 K, which is expected to reduce the phonon occupation numbers. In this case, as shown in Fig. 3, the electron localization in the $WSe_2$ layer only decreases by 20%, while the electron energy hardly changes in 1 ps, which is much slower than that at 300 K. Additionally, there is no charge oscillation. This results in a decrease of the oscillation amplitude of energy time-evolution as can be seen by comparing Fig. 2 (b) and (d), and as a result, the crossings between the $WSe_2$@K and $MoSe_2$@T disappear. Therefore the AD charge transfer between them is suppressed. There is still some crossing between $WSe_2$@K with a $MoSe_2$ state with higher energy where the AD charge transfer can take place.

The NA charge transfer is also suppressed by the decrease in temperature. This can be understood by inspecting the non-adiabatic couplings (NAC), which determines the hopping probability between different states. The NAC is defined as:

$$d_{jk} = \langle \varphi_j | \nabla_R | \varphi_k \rangle \cdot \dot{R} = \frac{\langle \varphi_k | \nabla_R H | \varphi_j \rangle}{\epsilon_k - \epsilon_j} \dot{R} \quad . \tag{3}$$

where $H$ is the Kohn-Sham Hamiltonian, $\varphi_k$, $\varphi_j$, $\epsilon_k$, $\epsilon_j$ are the corresponding wave functions and eigenvalues for electronic states *k* and *j*, and $\dot{R}$ is velocity of the nuclei.[63-65] Thus, NAC elements show strong dependence on the energy difference of the interacting states, the time-dependent orbital distribution of state *k* and *j*, i.e. the *e-p* matrix element,[66] and the nuclear velocity. All of these factors are related to *e-p* coupling and phonon excitation, and therefore are temperature dependent. As can be seen in Fig. 3 (e) and (g), when the temperature decreases from 300 to 100 K, the NAC between the initial ($WSe_2$@K) and final states ($MoSe_2$@T and $MoSe_2$@K) becomes negligible, which explains the insufficient NA charge transfer between them. The reduction of both the AD and NA charge transfer can be understood as phonon bottleneck effects. All of these temperature-dependent results unambiguously suggest that a phonon coupled coherent charge oscillation can be excited in $MoSe_2/WSe_2$ heterostructure through *e-p* coupling and that it can be suppressed through phonon reduction.

As a comparison, we perform additional NAMD calculations of the $MoS_2/WS_2$ heterostructure interface, where a similar electron transfer process is considered with the initial electron populated at $WS_2$@K. The results are significantly different from those in $MoSe_2/WSe_2$, as can be seen in Fig. 4. Here, the electron localization drops from 75% to nearly 0% within 1 ps at 300 K, and there is no charge oscillation in the electron transfer [Fig. 4 (a)]. Also, the charge transfer dynamics is much less dependent on the temperature. There is no qualitative change at 100 K, where the electron localization also drops from 90% to 35% in 1 ps [Fig. 4 (b)]. More analysis show that the charge transfer mainly occurs by NA mechanism at both 300 and 100 K [Fig. 4 (a-b)] in $MoS_2/WS_2$, indicating that the electron in $MoS_2/WS_2$ tends to relax by tunneling between donor and acceptor states rather than oscillate coherently with the phonon vibration. In the momentum space, the electron transfer proceeds by direct tunneling from $WS_2$@K to $MoS_2$@T and finally to $MoS_2$@K, as is shown in the schematics in Fig. 4 (f) and (h).

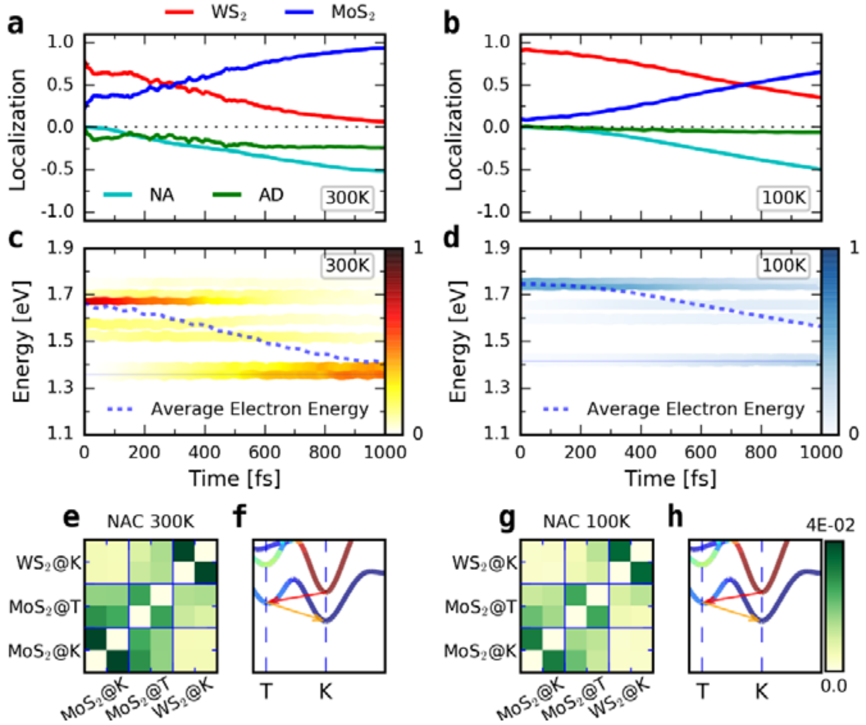

Figure 4. Non-adiabatic molecular dynamics results of $MoS_2/WS_2$ at 300 and 100 K, respectively. (a-b) Time-dependent electron spatial localization and (c-d) electron energy change at 300 and 100 K. In the upper part of (a-b) the red and blue lines shows the spatial electron localization on $WS_2$ and $MoS_2$ and in the lower part the green and cyan lines show the AD and NA contributions of the electron transfer. The color strips in (c-d) indicate electron distribution among different states and the dashed lines represent the averaged electron energy. The energy reference in (c-d) is the averaged energy of $WX_2$@K_VB while the average energy of $MoX_2/WX_2$ CBM is indicated by the horizontal line. (e) and (g) show the averaged non-adiabatic couplings (NAC) along 2 ps NAMD trajectory at 300 and 100 K. (f) and (h) show schematics of the electron relaxation route in the momentum space.

The distinct behaviors between the electron transfer of $MoS_2/WS_2$ and $MoSe_2/WSe_2$ can be understood from two perspectives. First, the $A_1$ phonon mode, which is the major mode coupled with excited electrons, has a relatively low frequency in $MoSe_2/WSe_2$ (230 $cm^{-1}$), and therefore, sufficient phonons can be excited at 300 K. Thus through *e-p* coupling, a strong phonon coupled coherent charge oscillation can be achieved in both energy evolution [Fig. 2 (d)] and spatial localization [Fig. 3 (a)]. By contrast, the frequency of $A_1$ mode in $MoS_2/WS_2$ is around 400 $cm^{-1}$ that is higher than that in $MoSe_2/WSe_2$, which makes the phonon occupation much smaller. Therefore the phonon coupled charge oscillation is suppressed. Second, the NAC elements between the donor ($WX_2$@K) and acceptor ($MoX_2$@T) states are larger in $MoS_2/WS_2$ than those in $MoSe/WSe_2$ at the same temperature. This is mainly because the energy difference between $WX_2$@K and $MoX_2$@T states is smaller in $MoS_2/WS_2$. Because of the large NAC and weak $A_1$ phonon excitation, charge transfer in $MoS_2/WS_2$ is dominated by the NA mechanism, where the charge prefers to tunnel between different states instead of coherent oscillation with the phonons. Therefore, the temperature effects in $MoS_2/WS_2$ are much less significant.

## D. Excitonic Effects Estimation

So far, our NAMD calculations essentially mimic the relaxation process of free photoexcited carriers, which is not the case in experiments where the photo-excited carriers exist in the form of bound electron-hole pairs, i.e. excitons. In this report, we use a simple method in the NAMD calculations where the excited electron energies are shifted according to the experimental value of optical absorption peaks of TMD heterostructures[51, 53] to estimate the possible excitonic effects. The energy shifting technique is known as the “scissor operator” method and has previously been used to correct band gap errors in DFT calculations.[67-69]

As schematically shown in Fig. 1 (c), the intralayer exciton is first formed at K point of $WX_2$ with the hole locate on $WX_2$@K in valance band ($WX_2$@K_VB) and electron on CBM of $WX_2$. Then the electron will transfer from the $WX_2$ CBM to the $MoX_2$ CBM, forming an interlayer exciton In this process, the hole stays unchanged on $WX_2$@K_VB. Therefore, by choosing the energy $WX_2$@K_VB as a reference, the position of $WX_2$ CBM is determined by the $WX_2$ intralayer band gap ($E_g$*_intra*) and the position $MoX_2$ CBM is determined by the $MoX_2/WX_2$ interlayer band gap ($E_g$*_inter*) as we indicate in Fig. 1 (a-b). Taking into account the exciton effects, $E_g$*_intra* and $E_g$*_inter* should be the optical band gaps instead of the quasiparticle band gaps. The optical band gaps $E_g$*_intra* of $WX_2$ and $E_g$*_inter* of $MoX_2/WX_2$ from different previous studies based on optical absorption spectra and GW+BSE calculations are summarized in Table S1 in the Supplemental Material[48]. We use the experimental optical band gaps of $WS_2$ and $WS_2/MoS_2$ from ref. [51] and that of $WSe_2$ and $WSe_2/MoSe_2$ from ref. [53] to correct the DFT band structure. The DFT and optical band gaps by absorption spectra, as well as their deviation are summarized in Table 1.

| | $E_g$*_inter* ($MoS_2/WS_2$) | $E_g$*_intra* ($WS_2$) | $\Delta E$ ($MoS_2/WS_2$) | $E_g$*_inter* ($MoSe_2/WSe_2$) | $E_g$*_intra* ($WSe_2$) | $\Delta E$ ($MoSe_2/WSe_2$) |
|---|---|---|---|---|---|---|
| Exp. | 1.94 [51] | 2.02 [51] | 0.08 | 1.35 [53] | 1.65 [53] | 0.3 |
| DFT | 1.45 | 1.75 | 0.3 | 1.22 | 1.52 | 0.3 |
| deviation | 0.49 | 0.27 | -0.22 | 0.13 | 0.13 | 0 |

Table 1 The values of interlayer band gap ($E_g$*_inter* of $MoX_2/WX_2$), intralayer band gap ($E_g$*_intra* for $WX_2$) and CBM energy offset ($\Delta E$) obtained by DFT and absorption spectra. The deviation between experimental and DFT results is also shown.

The excited electron dynamics is mostly affected by the CBM energy offset ($\Delta E$) of $WX_2$ and $MoX_2$ [indicated in Fig. 1 (a-b)], which is determined from the $E_g$*_intra* of $WX_2$ and $E_g$*_inter* of $MoX_2/WX_2$ as $\Delta E = E_g\_intra - E_g\_inter$. Using the experimental optical band gaps, $\Delta E$ is calculated to be 0.08 and 0.3 eV for $MoS_2/WS_2$ and $MoSe_2/WSe_2$ as shown in Table 1. In comparison, the $\Delta E$ obtained by DFT is 0.3 eV for both of them. Therefore, one can see that the energy shift due to exciton binding decrease the CBM energy offset of $MoS_2/WS_2$ significantly, while as for $MoSe_2/WSe_2$, it has little effect. As shown in the insets of Fig. 5 (e-f), due to the significant decrease of $\Delta E$ in $MoS_2/WS_2$, after the band shifting by the “scissor operator”, the

$WS_2$@K is moved below the $MoS_2$@T state. Since the excited electron has very little probability to transfer to a state with higher energy, the intervalley charge transfer route from $WS_2$@K to $MoS_2$@T is blocked. The excited electron can only decay from $WS_2$@K to $MoS_2$@K directly. Thus, the excited electrons at $WS_2$@K decay much slower both at 100 and 300 K as shown in Fig. 5.

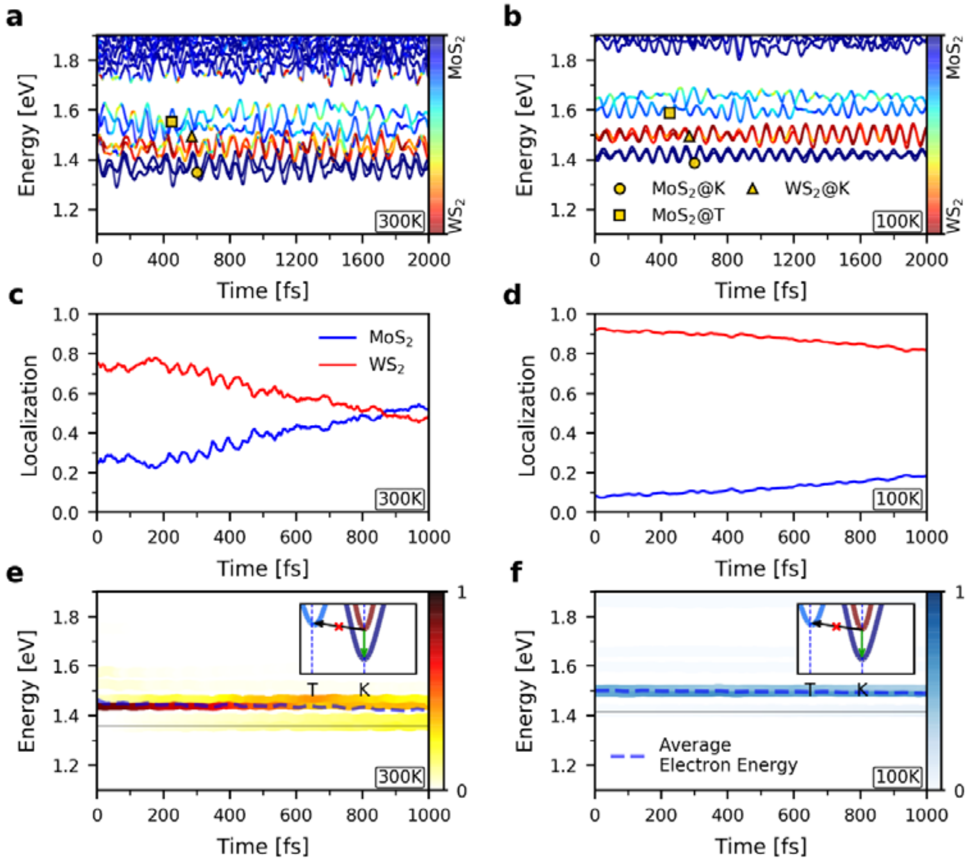

Figure 5. NAMD results after applying "scissor operator" for exciton effects. (a-b) Time evolutions of the energy states near CBM at 100 and 300 K. (c-d) Time-dependent electron spatial localization and (e-f) electron energy change at 100 and 300 K. The color strips in (e-f) indicate electron distribution among different states and the dashed lines represent the averaged electron energy. The energy reference in (c-d) is the averaged energy of $WX_2$@K_VB while the average energy of CBM is indicated by the horizontal line.

## E. Discussion

Taking $MoS_2/WS_2$ and $MoSe_2/WSe_2$ as prototype systems with good contrast, we found that phonon excitation is one crucial factor affecting the interlayer charge transfer, which can be tuned using different experimental techniques. The phonon excitation is strongly affected by the phonon frequency, which is determined by the chemical bonding strength. It can be tuned by changing the elements (for example S versus Se as we show in this report) or by applying external stress. For example, in 2D graphene and $MoS_2$, the phonons have been found to soften by application of a tensile stress.[70, 71] Further, recently the "phonon pumping" techniques using infrared light have been used to excite resonant lattice phonons and phonon-dressed electronic states.[72-76] With such a technique, we can expect that $A_1$ mode and the coherent charge oscillation in $MoSe_2/WSe_2$ can be selectively excited.

In this report, we use the "scissor operator" method to estimate the exciton effects on the electron transfer at $MoS_2/WS_2$ and $MoSe_2/WSe_2$ interface. It is needed to be clarified that in this method only the shift of energy is considered. The wave functions used to calculate the NA coupling is still on the DFT level. Based on this simple estimation, the electron transfer dynamics of $MoS_2/WS_2$ is possible to be significantly affected. More accurate treatments of the exciton effects are essential for the future study.

## Summary

To summarize, using *ab initio* NAMD, taking $MoS_2/WS_2$ and $MoSe_2/WSe_2$ which have similar band structures yet different phonon frequencies as prototype systems, we study the *e-p* coupling effects on the photo-excited interlayer electron transfer. We found that for both systems, the intralayer optical $A_1$ mode couples mostly with the electron dynamics. For $MoSe_2/WSe_2$, which has a lower $A_1$ phonon frequency, a phonon coupled charge oscillation can be excited at room temperature with sufficient phonon excitation. Such a charge oscillation is difficult to excite in $MoS_2/WS_2$ since the $A_1$ phonon frequency is higher the phonon excitation is more difficult. Such phonon excitation can be tuned by different experimental techniques and therefore the phonon coupled charge oscillation is possible to be controlled. The atomic level picture on how the phonons affect the interlayer charge transfer dynamics provides specific new insights for the fundamental understanding of ultrafast dynamics at vdW hetero-interfaces, and the design of novel quasi-2D devices for optoelectronic and solar energy conversion applications.

## Acknowledgements

This work is supported by NSFC (11620101003, 11704363, 21421063), by National Key Basic Research Program of China (2016YFA0200604, 2017YFA0204904), the Fundamental Research Funds for the Central Universities WK3510000005. WAS acknowledges a startup fund from the University of Pittsburgh. O.V.P. acknowledges financial support of the U.S. National Science Foundation, Grant No. CHE-1565704. Calculations were performed at Environmental Molecular Sciences Laboratory at the PNNL, a user facility sponsored by the DOE Office of Biological and Environmental Research and USTC supercomputing center. We thank Z. Zhang and J. Yang for valuable discussions.

[1] K. F. Mak, C. Lee, J. Hone, J. Shan, and T. F. Heinz, *Phys. Rev. Lett.*, **105**, (2010).

[2] K. F. Mak, K. He, J. Shan, and T. F. Heinz, *Nat. Nanotechnol.*, **7**, 494-8 (2012).

[3] G. Eda, H. Yamaguchi, D. Voiry, T. Fujita, M. Chen, and M. Chhowalla, *Nano Lett.*, **11**, 5111-5116 (2011).

[4] T. Cheiwchanchamnangij and W. R. L. Lambrecht, *Phys. Rev. B*, **85**, 205302 (2012).

[5] A. Ramasubramaniam, *Phys. Rev. B*, **86**, 115409 (2012).

[6] M. Bernardi, M. Palummo, and J. C. Grossman, *Nano Lett.*, **13**, 3664-3670 (2013).

[7] P. Rivera, K. L. Seyler, H. Yu, J. R. Schaibley, J. Yan, D. G. Mandrus, W. Yao, and X. Xu, *Science*, **351**, 688-691 (2016).

[8] X. Wang and F. Xia, *Nat. Mater.*, **14**, 264-265 (2015).

[9] X. Hong, et al., *Nat. Nanotechnol.*, **9**, 682-686 (2014).

[10] L. Britnell, et al., *Science*, **340**, 1311-1314 (2013).

[11] F. Withers, et al., *Nat. Mater.*, **14**, 301-306 (2015).

[12] W. J. Yu, Y. Liu, H. Zhou, A. Yin, Z. Li, Y. Huang, and X. Duan, *Nat. Nanotechnol.*, **8**, 952-958 (2013).

[13] Q. H. Wang, K. Kalantar-Zadeh, A. Kis, J. N. Coleman, and M. S. Strano, *Nat. Nanotechnol.*, **7**, 699-712 (2012).

[14] J. Feng, X. Qian, C.-W. Huang, and J. Li, *Nat. Photon.*, **6**, 866-872 (2012).

[15] J. Kang, S. Tongay, J. Zhou, J. Li, and J. Wu, *Appl. Phys. Lett.*, **102**, 012111 (2013).

[16] C. Gong, H. Zhang, W. Wang, L. Colombo, R. M. Wallace, and K. Cho, *Appl. Phys. Lett.*, **103**, 053513 (2013).

[17] H.-P. Komsa and A. V. Krasheninnikov, *Phys. Rev. B*, **88**, 085318 (2013).

[18] H. Terrones, F. López-Urías, and M. Terrones, *Sci. Rep.*, **3**, 1549 (2013).

[19] K. Kośmider and J. Fernández-Rossier, *Phys. Rev. B*, **87**, 075451 (2013).

[20] D. Y. Qiu, F. H. da Jornada, and S. G. Louie, *Phys. Rev. Lett.*, **111**, 216805 (2013).

[21] A. M. Jones, et al., *Nat. Nanotechnol.*, **8**, 634-638 (2013).

[22] M. M. Ugeda, et al., *Nat. Mater.*, **13**, 1091-1095 (2014).

[23] F. Ceballos, M. Z. Bellus, H.-Y. Chiu, and H. Zhao, *ACS Nano*, **8**, 12717-12724 (2014).

[24] X. Zhu, N. R. Monahan, Z. Gong, H. Zhu, K. W. Williams, and C. A. Nelson, *J. Am. Chem. Soc.*, **137**, 8313-8320 (2015).

[25] C.-H. Lee, et al., *Nat. Nanotechnol.*, **9**, 676-681 (2014).

[26] H. Wang, J. Bang, Y. Sun, L. Liang, D. West, V. Meunier, and S. Zhang, *Nat. Commun.*, **7**, 11504 (2016).

[27] R. Long and O. V. Prezhdo, *Nano Lett.*, **16**, 1996-2003 (2016).

[28] Q. Zheng, W. A. Saidi, Y. Xie, Z. Lan, O. V. Prezhdo, H. Petek, and J. Zhao, *Nano Lett.*, **17**, 6435-6442 (2017).

[29] Z. Ji, et al., *ACS Nano*, **11**, 12020-12026 (2017).

[30] G. Moody, J. Schaibley, and X. Xu, *J. Opt. Soc. Am. B*, **33**, C39 (2016).

[31] W. R. Duncan and O. V. Prezhdo, *Annu. Rev. Phys. Chem.*, **58**, 143-184 (2007).

[32] C. F. Craig, W. R. Duncan, and O. V. Prezhdo, *Phys. Rev. Lett.*, **95**, 163001 (2005).

[33] L. Wang, R. Long, and O. V. Prezhdo, *Annu. Rev. Phys. Chem.*, **66**, 549-579 (2015).

[34] O. V. Prezhdo, W. R. Duncan, and V. V. Prezhdo, *Prog. Surf. Sci.*, **84**, 30-68 (2009).

[35] O. V. Prezhdo, W. R. Duncan, and V. V. Prezhdo, *Acc. Chem. Res.*, **41**, 339-348 (2008).

[36] W. Chu, W. A. Saidi, Q. Zheng, Y. Xie, Z. Lan, O. V. Prezhdo, H. Petek, and J. Zhao, *J. Am. Chem. Soc.*, **138**, 13740-13749 (2016).

[37] C. Zhao, Q. Zheng, J. Wu, and J. Zhao, *Phys. Rev. B*, **96**, 134308 (2017).

[38] http://staff.ustc.edu.cn/~zhaojin/code.html,

[39] G. Kresse and J. Hafner, *Phys. Rev. B*, **47**, 558-561 (1993).

[40] G. Kresse and J. Hafner, *Phys. Rev. B*, **48**, 13115-13118 (1993).

[41] G. Kresse and J. Hafner, *Phys. Rev. B*, **49**, 14251-14269 (1994).

[42] G. Kresse and J. Furthmüller, *Phys. Rev. B*, **54**, 11169-11186 (1996).

[43] A. V. Akimov and O. V. Prezhdo, *J. Chem. Theo. Comput.*, **9**, 4959-4972 (2013).

[44] A. V. Akimov and O. V. Prezhdo, *J. Chem. Theo. Comput.*, **10**, 789-804 (2014).

[45] G. Kresse and D. Joubert, *Phys. Rev. B*, **59**, 1758-1775 (1999).

[46] J. P. Perdew, K. Burke, and M. Ernzerhof, *Phys. Rev. Lett.*, **77**, 3865-3868 (1996).

[47] S. Grimme, *J. Comput. Chem.*, **27**, 1787-1799 (2006).

[48] See Supplemental Material at [URL] for more details of the calculation method, the selection of supercell and k-points, the discussion of spin orbit coupling effects, stacking effects, k-point grid effects and different-functional effects.

[49] P. E. Blöchl, *Phys. Rev. B*, **50**, 17953-17979 (1994).

[50] J. C. Tully, *J. Chem. Phys.*, **93**, 1061-1071 (1990).

[51] J. Zhang, et al., *Adv. Mater.*, **28**, 1950-1956 (2016).

[52] B. Zhu, X. Chen, and X. Cui, *Sci. Rep.*, **5**, 9218 (2015).

[53] P. Rivera, et al., *Nat. Commun.*, **6**, 6242 (2015).

[54] A. Chernikov, T. C. Berkelbach, H. M. Hill, A. Rigosi, Y. Li, O. B. Aslan, D. R. Reichman, M. S. Hybertsen, and T. F. Heinz, *Phys. Rev. Lett.*, **113**, 076802 (2014).

[55] Z. Ye, T. Cao, K. O'Brien, H. Zhu, X. Yin, Y. Wang, S. G. Louie, and X. Zhang, *Nature*, **513**, 214-218 (2014).

[56] H. Yu, Y. Wang, Q. Tong, X. Xu, and W. Yao, *Phys. Rev. Lett.*, **115**, 187002 (2015).

[57] H. Heo, et al., *Nat. Commun.*, **6**, 7372 (2015).

[58] P. K. Nayak, et al., *ACS Nano*, **11**, 4041-4050 (2017).

[59] P. Nagler, et al., *Nat. Commun.*, **8**, 1551 (2017).

[60] Y. Gong, et al., *Nat. Mater.*, **13**, 1135-1142 (2014).

[61] S. V. Bhatt, M. P. Deshpande, V. Sathe, R. Rao, and S. H. Chaki, *J. Raman Spec.*, **45**, 971-979 (2014).

[62] B. Amin, T. P. Kaloni, G. Schreckenbach, and M. S. Freund, *Appl. Phys. Lett.*, **108**, 063105 (2016).

[63] I. Tavernelli, B. F. E. Curchod, and U. Rothlisberger, *J. Chem. Phys.*, **131**, 196101 (2009).

[64] C. Hu, H. Hirai, and O. Sugino, *J. Chem. Phys.*, **128**, 154111 (2008).

[65] K. G. Reeves, A. Schleife, A. A. Correa, and Y. Kanai, *Nano Lett.*, **15**, 6429-6433 (2015).

[66]G. Grimvall, *The Electron-Phonon Interaction in Metals*, (North-Holland, New York), Selected Topics in Solid State Physics

[67] R. W. Godby, M. Schlüter, and L. J. Sham, *Phys. Rev. B*, **37**, 10159-10175 (1988).

[68] F. Gygi and A. Baldereschi, *Phys. Rev. Lett.*, **62**, 2160-2163 (1989).

[69] K. A. Johnson and N. W. Ashcroft, *Phys. Rev. B*, **58**, 15548-15556 (1998).

[70] F. Liu, P. Ming, and J. Li, *Phys. Rev. B*, **76**, 064120 (2007).

[71] T. Li, *Phys. Rev. B*, **85**, 235407 (2012).

[72] W. Hu, et al., *Nat. Mater.*, **13**, 705-711 (2014).

[73] M. Mitrano, et al., *Nature*, **530**, 461-464 (2016).

[74] Y. H. Wang, H. Steinberg, P. Jarillo-Herrero, and N. Gedik, *Science*, **342**, 453-457 (2013).

[75] I. Gierz, et al., *Phys. Rev. Lett.*, **115**, 086803 (2015).

[76] E. Pomarico, et al., *Phys. Rev. B*, **95**, 024304 (2017).